A Semi-Consensus Strategy Toward Multi-Functional Hybrid Energy Storage System in DC Microgrids

Pengfeng Lin, *Student Member, IEEE*, Tianyang Zhao, *Member, IEEE*, Benfei Wang, *Member, IEEE*, Yu Wang, *Member, IEEE*, and Peng Wang, *Fellow, IEEE*

***Abstract*—This paper proposes a semi-consensus strategy for multi-functional hybrid energy storage systems (HESSs) in DC microgrids. Batteries in a HESS are regulated by conventional V-P droops and supercapacitors (SCs) are with integral droops (ID). Only batteries are assigned with local distributed compensators which exchange information through sparse communication links. Those SCs are exempted from data exchange process, which would save system investment costs. Within the semi-consensus scheme, the most essential function is the cooperation of V-P droop and ID that helps to naturally allocate low frequency components of load power to batteries and high frequency components to SCs, thus prolonging the overall life time of HESS. In addition to the transient power allocation function, there are other three functions endowed by the proposed strategy, which are autonomous DC bus voltage recovery to its nominal level, spontaneous SC state of charge (SOC) restoration, autonomous power sharing and SOC balancing among batteries. It is the simultaneous realization of above four functions with limit communications that makes up the main contributions in this paper. A generic mathematical modeling of HESS with the semi-consensus strategy is established. The model allows for dynamic analyses to theoretically validate the effectiveness of proposed method in both frequency and time domains. In-house experimental results are shown fully consistent with the dynamic analyses and also effectively corroborate the intended HESS multi-functional operations.**

***Index Terms*—Hybrid energy storage system, semi-consensus strategy, multi-functional operations, DC microgrids.**

I. Introduction

TECHNOLOGICAL advancements in power electronics have substantially boosted the utilization of power converter based DC renewable resources (RESs) and DC-compatible energy storages (ESs) in electrical power systems. DC microgrids (MGs) could provide a decent way to incorporate those RESs and ESs to desirably manage their powers and achieve lower operation loss by using less energy conversion stages. Besides, a DC MG circumvents problems of synchronization, reactive powers and harmonics, which may always degrade power quality in its AC counterparts. Normally, the DC MG could work in grid connected mode and islanded mode. For the former, the MG is supported by a utility grid of a much larger capacity which entails the MG strong enough to accommodate various harsh conditions. If the utility is in faults, the DC system should disconnect from the grid immediately and work in islanded mode. For this mode, ESs are normally configured to regulate DC bus voltage and compensate the power mismatch between RESs and loads.

Note that ESs would comprise heterogeneous types of energy storages that differ in dynamic performances. Specifically, batteries are of high energy density but low power density, whereas supercapacitors (SCs) storing energy in electrical way, theoretically feature infinite power density but limited energy density. For a given loading profile, it is preferred that those batteries compensate the smoothly-changing components of load, and SCs respond to the fast load variations, which forms a hybrid energy storage system (HESS) [1]. To this end, a plethora of control strategies have been studied in the literature.

The first family of HESS control strategy refers to decentralized controls. The decentralized approaches do not rely on any communication infrastructure, intending to enhance MG scalability. For examples, in [2], a high-pass filter (HPF) and a low-pass filter (LPF) are integrated into a HESS for splitting the load power into high and low frequency components. Reference [3] suggests to apply LPFs to those ESs with slow responses, while other ESs automatically cover the high frequency parts of load power. In [4], inspired by charging and discharging processes of capacitors, an novel integral droop (ID) controller is proposed to regulate the output voltage of SC interfaced converter. Then a HPF and a LPF are naturally formulated to correctly decompose the demanded load power. Similar efforts can also be found in [5] where a revised virtual impedance is investigated for transient power sharing. To avoid SC state of charge (SOC) depletion, a simple integrator is implemented in SC converter for the self-driven SOC restoration [6].

The second family for HESS management methods comes to centralized controls, where a central controller exists collecting information across the whole MG through communication and allows numerous control scheme being flexibly practiced. In [7], a model predictive control (MPC) coordinating mechanism

Manuscript received March 31, 2019; revised July 7, 2019; accepted August 14, 2019. Date of publication August 19, 2019; date of current version February 19, 2020. This work was supported by Project Renewable Energy Integration Demonstrator-Singapore in Energy Research Institute at Nanyang Technological University, Singapore. Paper no. TEC-00335-2019. *(Corresponding author: Yu Wang.)*

P. Lin and T. Zhao are with the Energy Research Institute, Nanyang Technological University, Singapore 637141 (e-mail: linp0010@e.ntu.edu.sg; zhaoty@ntu.edu.sg).

B. Wang is with the School of Intelligent Systems Engineering, Sun Yat-sen University, Shenzhen 510275, China (e-mail: wbfsysu@163.com).

Y. Wang is with the Rolls-Royce@NTU Corporate Lab, Nanyang Technological University, Singapore 639798 (e-mail: wang_yu@ntu.edu.sg).

P. Wang is with the School of Electrical and Electronic Engineering, Nanyang Technological University, Singapore 639798 (e-mail: epwang@ntu.edu.sg).

Color versions of one or more of the figures in this article are available online at http://ieeexplore.ieee.org.

Digital Object Identifier 10.1109/TEC.2019.2936120

is studied, which generates high frequency and low frequency power references for batteries and SCs respectively in a centralized fashion. A remote console desk based on PLC (programmable logic controller) is reported in [8] to real-time schedule ESs powers for attaining DC MG optimal operations. A deadbeat method is presented in [9] to orchestrate the functioning of batteries and SCs by generating optimal duty ratios for DC/DC converters. Similar to [7], a model predictive current controller is investigated in [10], and the cooperations of storages is achieved by a bidirectional three level converter.

Notice that the DC bus voltage deviation in the decentralized scheme would easily stretch out of the allowable range, which may cause damages to those voltage-sensitive loads. The proper power sharing and SOC balancing among ESs would also be impaired if individual storages are blind to the operating status of others. Although these difficulties can be accordingly addressed by centralized controls, the existences of central controllers are universally criticized being vulnerable to single-point-failures which mean that the failures of specific parts will stop the entire DC system from regular working [11], [12]. As an alternative solution to centralized methods, distributed controls take the advantage of realizing advanced energy management strategies devoid of central controllers via sparse communication links. As stated in [13], distributed patterns are demonstrated being robust against communication losses. In the realm of HESS applications, typical distributed controls are applied to diversified battery packs where no droop control is adopted [14]. This means the DC MG will definitely undergo collapse in the case of data network outage. The same controller is subsequently implemented in [15] for MG performance improvements, and ESs are thereby billed as electrical springs. A distributed secondary control is exhibited in [16] for restoring DC bus voltage to its nominal value and ensuring proportional power sharing in batteries. A hybrid discrete-continuous consensus in [17] is shown to achieve the same objectives in [16] while possibly reducing computational burdens. However, it is essential to pinpoint that the strategies in [15]–[17] share the identical shortcoming of neglecting the transient power allocation in HESSs. This may compromise the lifespan and dynamic responses of HESSs.

To obtain better power management in a particular HESS and prolong its life expectation, a novel semi-consensus strategy is proposed for HESS multi-functional operations. For SCs, their SOCs which represent the remaining stored energy [18], will be easily depleted if they are continuously discharged. Benefiting from fast dynamics, SCs are more likely supposed to only absorb transient load changes and stop short of supplying power in steady state. As such, it is highly recommended to install SCs close to the DC bus for escalating the bus buffering capability. Then the impedances between SCs and the bus would be sufficiently small that can be overlooked. For batteries, they may be deployed in different sites feeding the DC bus via line impedances, and the power sharing and SOC balancing would not comply to the predefined pattern because of incommensurate discharging. In this context, distributed communication links are merely established among batteries, whereas SCs function in completely decentralized manners, which gives rise to the term "semi-consensus strategy" in this paper. Compared to the works wherein all ESs require exchanging data [19], [20], the proposed semi-consensus approach constructs communication networks only for parts of ESs, which certainly helps to save the capital costs for HESS. Furthermore, the multiple functions bestowed by semi-consensus strategy can be summarized as the following:

1) Transient power allocation between batteries and SCs. Batteries are equipped with V-P droops and SCs are with ID as in [4]. Then the high frequency components of load power can be autonomously allocated to SCs, while the low frequency parts are compensated by batteries. After system transition, SC powers gradually reduce to zero and SCs keep in idle states waiting for the next load change. Batteries fully feed the load power in the steady state; they would avoid releasing surge power in transitions. Compared with existing transient power decomposition methods that are only realized in a central controller, the ID can work in a fully autonomous way which means the central controller can be avoided.
2) Autonomous DC bus voltage recovery. Existence of droops may cause DC bus voltage largely deviating from its nominal value. To recover the DC bus voltage, distributed controllers are applied to batteries (but not SCs) such that in-service batteries could actively participate in bus voltage regulations. Note that SCs would not control the DC bus since the proposed strategy intends to render SCs only responding to transient power demand, thus enabling SCs to work in a long run without worrying SC SOC depletion.
3) Spontaneous SC SOC restorations. SCs are normally of high capacitances. For a particular amount of stored energy, their tolerable terminal voltage would be rather low. SCs could hence be coupled to the DC bus through converters which would adapt the SCs to fit the DC bus voltage. By assigning IDs to SCs, upon the DC bus voltage recovery, the dynamic powers released by SCs will spontaneously reflow to SCs. For the entire transition, no energy in SCs is conveyed to the load and SC SOCs will thus spontaneously maintain at the original values.
4) Autonomous power sharing and SOC balancing in batteries. For batteries, mismatched line impedances would induce inaccurate power sharing, and battery SOCs may also be different from one another due to uneven initial conditions. To balance the battery SOCs and enforce proportional power sharing, additional to voltage recovery control, another distributed controller is designed and executed to provide correction items for revising V-P droops. With this way will battery pack bears longer lifetime, and the autonomy of holistic HESS could also be strengthened.

The remainder of this paper is organized as follows. Section II gives the generalized DC MG and HESS configurations, and semi-consensus control architecture will also be meticulously illustrated. Section III derives the generic HESS mathematical model under the proposed scheme. Theoretical deductions for the preceding multi-functions and dynamic analyses are all conducted in

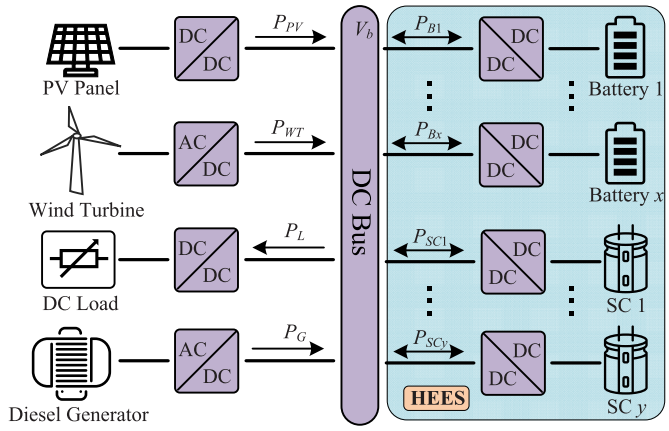

Fig. 1. A typical autonomous DC MG.

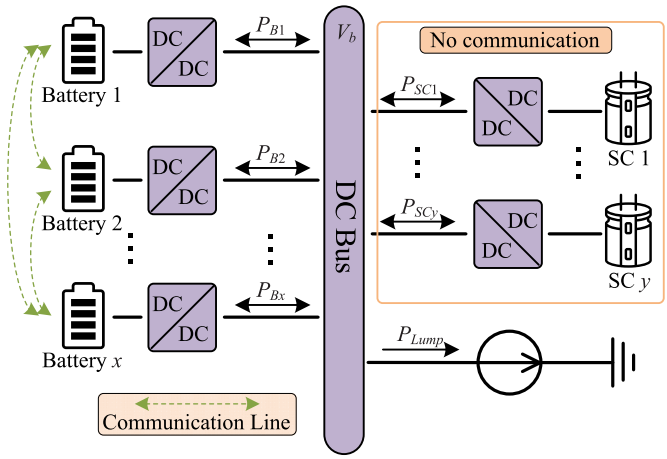

Fig. 2. A generalized HESS configuration.

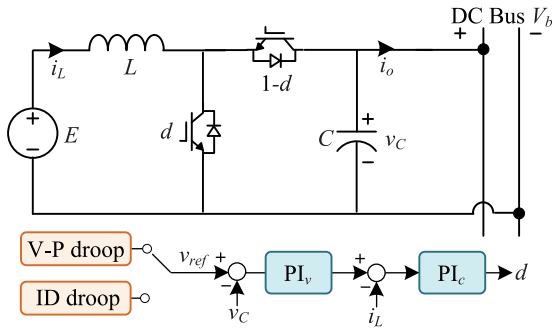

Fig. 3. A boost type interfacing converter for batteries and SCs.

Section IV. The effectiveness of semi-consensus strategy would be verified by hardware experiments in Section V. Finally, conclusions are drawn in Section VI.

II. Semi-Consensus Strategy for HESS in DC MG

In this section, DC MG and HESS system constructions are elaborated, based on which the detailed control mechanisms under the semi-consensus strategy will be illustrated.

A. System Configuration

Fig. 1 shows a typical autonomous DC MG. V_b represents DC bus voltage. PV panel and wind turbine (WT) are RESs working in maximum point point tracking modes. Diesel generator (DG) is linked the DC bus through an AC/DC rectifier, and DC load absorbs power via a DC/DC converter. A HESS consisting of x batteries and y SCs has been highlighted in Fig. 1. The HESS would help to address the power mismatch between the load consumption and the generation of PV, WT and DG. As this paper focuses on ESs coordination, the power mismatch can be collectively defined as a lumped load (P_{Lump}) from the perspective of HESS, i.e.,

$$P_{Lump} = P_L - P_G - P_{PV} - P_{WT}. \tag{1}$$

where P_L is load power. P_G, P_{PV} and P_{WT} stand for the powers from DG, PV and WT respectively.

A simplified version of Fig. 1 is shown in Fig. 2 where the xth battery power and the yth SC power are denoted as P_{Bx} and P_{SCy} respectively. The summation of battery and SC powers in Fig. 2 would equal P_{Lump} at any time, i.e.,

$$\sum_{i=1}^{x} P_{Bi} + \sum_{i=1}^{y} P_{SCj} = P_{Lump}. \tag{2}$$

B. Proposed Semi-Consensus Strategy

As in the introduction, batteries and SCs are assigned with V-P and ID droop controllers. These droops produce voltage references $V_{ref}s$ for the inner controllers of ES-interfacing converters. For instance, in Fig. 3, V_{ref} could be from either V-P or ID droop. Then V_{ref} is compared with the converter real output voltage v_C. The corresponding voltage error is processed by a proportional-integral (PI) controller which further generates the reference for inductor current i_L. Another PI would process the current error and give the control signal to drive the converter switches. Consequently, v_C will closely track V_{ref} in steady state. It is crucial to clarify that the input voltage E in Fig. 3 stands for the terminal voltage of either a battery or a SC. Optimal designs of the two PI controllers have commendably explicated in [4] for guaranteeing suitable converter dynamics and stability margins. Since those inner PI loops bear much higher bandwidths, as comprehended from [21], they can be viewed as unity gains and hence, the overall converter characteristic is dominated by droop equations. The V-P and ID droops for th ith battery and the ith SCs can be written below,

$$V_{ref} = V_{th} - m_i P_{Bi},\ m_i = \frac{\Delta V_{\max}}{P_{Bi\max}},\quad i = 1, 2, \ldots, x, \tag{3}$$

$$V_{ref} = V_{th} - n_i \frac{P_{SCi}}{s},\quad i = 1, 2, \ldots, y, \tag{4}$$

where s is Laplace operator. V_{th} is MG nominal voltage. $\Delta V_{\max}$ is the allowable maximum voltage deviation. $P_{Bi\max}$ is the rated power of the ith battery. m_i and n_j are droop coefficients of the battery and SC respectively. In light of (3) and (4), the consolidated droops for battery cluster and SC cluster can be

given as

$$V_{ref} = V_{th} - m_{eq}P_B, \quad P_B = \sum_{i=1}^{x} P_{Bi},$$
$$V_{ref} = V_{th} - n_{eq}\frac{P_{SC}}{s}, \quad P_{SC} = \sum_{i=1}^{y} P_{SCi}, \tag{5}$$

where $m_{eq} = (\sum_{i=1}^{x} m_i)^{-1}$ and $n_{eq} = (\sum_{i=1}^{y} n_i)^{-1}$ are the equivalent droop coefficients of battery and SC clusters whose out powers are expressed as P_B and P_{SC} respectively. Further considering $P_{SC} + P_B = P_{Lump}$, the power sharing between battery cluster and SC cluster can be described below [4],

$$P_B = \frac{n_{eq}/m_{eq}}{s + n_{eq}/m_{eq}} P_{Lump},$$
$$P_{SC} = \frac{s}{s + n_{eq}/m_{eq}} P_{Lump}. \tag{6}$$

It is shown in (6) that the HPF and LPF for spitting the load power are naturally formed. All batteries compensate the low frequency components of the load power whereas all SCs cover the high frequency parts. The power sharing among batteries would be inversely proportional to their droop coefficients,

$$P_{B1} : \cdots P_{Bi} : \cdots P_{Bx} = m_1^{-1} : \cdots m_i^{-1} : \cdots m_x^{-1}. \tag{7}$$

Similarly, SCs could perceive the common DC bus voltage, and the transient powers supplied by SCs comply to (8),

$$P_{SC1} : \cdots P_{SCi} : \cdots P_{SCy} = n_1^{-1} : \cdots n_i^{-1} : \cdots n_y^{-1}. \tag{8}$$

To make full use of SC advantages of buffering energy, as emphasize previously, SCs are suggested to install rightly at the DC bus. However, those batteries of larger energy capacities are more than likely to locate at different places which would be coupled with DC bus through line impedances. The mismatched line impedances may jeopardize the battery power sharing accuracy. This inaccuracy together with unequal initial charging conditions will further aggravate battery SOCs balance in real-time operations. Moreover, the floating bus voltage should also be appositely regulated and restored to its nominal value for enhancing DC power qualities. Responding to these issues, a sparse communication network is built and applied to the battery cluster in Fig. 2, and no data exchanging will be incurred in SCs. With semi-consensus strategy, the droop equation of the ith battery is superposed by two correction items, δ_i and ε_i, generated by its local distributed compensators. The detailed schematics of the compensators are displayed in Fig. 4. δ_i and ε_i subject to the below differential equations,

$$\dot{\delta}_i = \alpha_i e_{Vi}, \quad \dot{\varepsilon}_i = \beta_i e_{Pi},$$
$$e_{Vi} = g_i\,(V_{th} - V_b) + \sum_j (\delta_j - \delta_i),$$
$$e_{Pi} = \sum_j (P_{Bj}/P_{Bj\max} - P_{Bi}/P_{Bi\max}) + \gamma_i \sum_j (\mathrm{SOC}_{Bi} - \mathrm{SOC}_{Bj}), \tag{9}$$

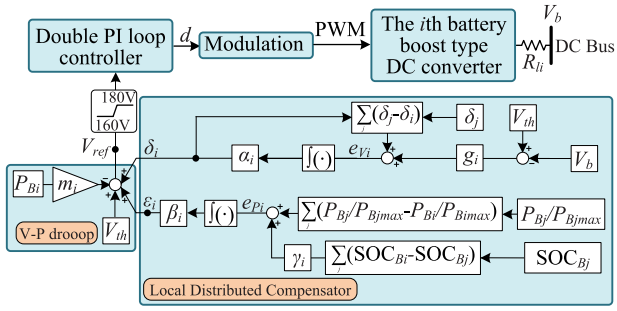

Fig. 4. The schematic of local distributed compensator for the ith battery.

where δ_i, SOC_{Bi} and $P_{Bi}/P_{Bi\max}$ are the data that are locally accessible. δ_j, SOC_{Bj} and $P_{Bj}/P_{Bj\max}$ are signals transmitted from the neighbors of the ith battery. α_i, β_i and γ_i are constants. g_i is a pinning gain which could be either one or zero, as explained in [16]. It is worth noting that the voltage restoration process can be viewed as the tracking issue since the HESS bus voltage is expected to stabilize at V_{th}. Hence, the pinning gain g_i is involved for generating δ_i. For ε_i, the intention is to balance the rated power quantities and SOCs, which can be identified as an averaging process, thereby not necessary to incorporate g_i. For γ_i, if increased, the weight of SOC balancing in formulating β_i will be boosted and the SOC balancing process among batteries would be expedited. However, it is also possible to reduce γ_i so that the balancing process could be slowed down, which may prohibit a certain battery from absorbing power and avoid unnecessary power losses.

In the ith battery, its SOC is below [9],

$$\mathrm{SOC}_{Bi} = \mathrm{SOC}_{Bi0} - \int_0^t \frac{P_{Bi}}{E_{Bi}^{rate}} dt, \tag{10}$$

where SOC_{Bi0} and E_{Bi}^{rate} are the initial battery SOC and the rated energy respectively. After knowing the two correction items, the V-P droop formula in (3) can hereby be updated as

$$V_{ref} = V_{th} - m_i P_{Bi} + \delta_i + \varepsilon_i. \tag{11}$$

Notice that the ID droop equation in (4) would keep unchanged as intended. Intuitively, observing (9) reveals that the two errors pertaining to the differences in voltages, intermediate variables δ, nominated battery powers and SOCs, will all be zero in steady state due to the strong regulation of signal integrations. Then the following expressions would hold,

$$V_b = V_{th}, \ \frac{P_{B1}}{P_{B2\max}} = \cdots \frac{P_{Bi}}{P_{Bi\max}} = \cdots \frac{P_{Bx}}{P_{Bx\max}},$$
$$\mathrm{SOC}_{B1} = \cdots \mathrm{SOC}_{Bi} = \cdots \mathrm{SOC}_{Bx}. \tag{12}$$

Eq. (12) shows that the bus voltage restoration, proportion power sharing and SOC balancing in batteries have all been realized under the proposed semi-consensus strategy. Along with V_b recovery, the SOCs of SCs can also be retrieved to the initial values. For clear explanations, resembling (10) and

ignoring converter loss [6], the ith SC has its SOC delineated as

$$\mathrm{SOC}_{SCi} = \mathrm{SOC}_{SCi0} - \int_0^t \frac{P_{SCi}}{E_{SCi}^{rate}} dt, \tag{13}$$

where SOC_{SCi0} and E_{SCi}^{rate} are the initial SOC and the rated energy of SC. In steady state, V_{ref} in (4) equals V_b. Considering the results in (12), $V_b = V_{th}$, it comes that V_{ref} and V_{th} in (4) are favorably equalized. Rearranging (4) into time domain gives,

$$-(V_{ref} - V_{th})/n_i = \int_0^t P_{SCi} dt = 0. \tag{14}$$

Provided that E_{SCi}^{rate} is a constant, substituting (14) into (13) yields $\mathrm{SOC}_{SCi} = \mathrm{SOC}_{SC0}$. This means the SC SOC would not either increase or decrease. The SOC spontaneously maintains at its initial level after system transition, which allows for SC continuous operations without worrying about SOC depletion. Although the reasoning from (9) to (14) proclaims that the stipulated four functions of HESS have been accomplished, the reasoning is founded on the assumption that the dynamics, $\dot{\delta}_i$ and $\dot{\varepsilon}_i$ in (9), would decay to zero in steady state. To justify this assumption, the generic modeling for HESS with semi-consensus strategy would be performed in the next section, and pertinent dynamic analyses will also be provided.

III. HESS Generic Modeling

In this section, V_{ref} in (4) and (11) are displaced by V_b for simplicity. The compact forms of (4) and (11) can then be written as

$$\mathbf{1}_x V_b = \mathbf{1}_x V_{th} - \boldsymbol{m}\boldsymbol{P}_B + \boldsymbol{\delta} + \boldsymbol{\varepsilon}, \tag{15}$$

$$\mathbf{1}_y V_b = \mathbf{1}_y V_{th} - (s\boldsymbol{I}_y)^{-1}\boldsymbol{n}\boldsymbol{P}_{SC}, \tag{16}$$

where $\boldsymbol{V}_{th} = \mathbf{1}_x V_{th}$, $\boldsymbol{m} = diag(m_1 \cdots m_i \cdots m_x)$, $\boldsymbol{P}_B = col(P_{B1} \cdots P_{Bi} \cdots P_{Bx})$, $\boldsymbol{\delta} = col(\delta_1 \cdots \delta_i \cdots \delta_x)$, $\boldsymbol{\varepsilon} = col(\varepsilon_1 \cdots \varepsilon_i \cdots \varepsilon_x)$, $\boldsymbol{n} = diag(n_1 \cdots n_i \cdots n_y)$, $\boldsymbol{P}_{SC} = col(P_{SC1} \cdots P_{SCi} \cdots P_{SCy})$. $\boldsymbol{I}_y$ is an identity matrix. $\mathbf{1}_x$ and $\mathbf{1}_y$ are column vectors with all elements being 1.

For $\boldsymbol{\delta}$ and $\boldsymbol{\varepsilon}$, their corresponding equations in both time domain and s domain are expressed below,

$$\begin{aligned}
&t\ domain: \dot{\boldsymbol{\delta}} = \boldsymbol{\alpha}[\boldsymbol{G}\mathbf{1}_x(V_{th} - V_b) - \boldsymbol{L}\boldsymbol{\delta}],\\
&s\ domain: \boldsymbol{\delta} = \boldsymbol{A}(V_{th} - V_b),\\
&\qquad\qquad \boldsymbol{A} = (s\boldsymbol{I}_x + \boldsymbol{\alpha}\boldsymbol{L})^{-1}\boldsymbol{\alpha}\boldsymbol{G}\mathbf{1}_x,
\end{aligned} \tag{17}$$

$$\begin{aligned}
&t\ domain: \dot{\boldsymbol{\varepsilon}} = \boldsymbol{\beta}[-\boldsymbol{L}\boldsymbol{P}_{B\max}^{-1}\boldsymbol{P}_B + \boldsymbol{\gamma}\boldsymbol{L}\mathrm{SOC}_B],\\
&s\ domain: \boldsymbol{\varepsilon} = \boldsymbol{B}\boldsymbol{P}_B + \boldsymbol{C}\mathrm{SOC}_B,\\
&\qquad\qquad \boldsymbol{B} = -(s\boldsymbol{I}_x)^{-1}\boldsymbol{\beta}\boldsymbol{L}\boldsymbol{P}_{B\max}^{-1},\\
&\qquad\qquad \boldsymbol{C} = (s\boldsymbol{I}_x)^{-1}\boldsymbol{\beta}\boldsymbol{\gamma}\boldsymbol{L},
\end{aligned} \tag{18}$$

where $\boldsymbol{L}$ is Laplacian matrix that describes HESS communication structures in Fig. 2 [13]. $\boldsymbol{G} = diag(g_1 \cdots g_i \cdots g_x)$, $\boldsymbol{\alpha} = diag(\alpha_1 \cdots \alpha_i \cdots \alpha_x)$, $\boldsymbol{\beta} = diag(\beta_1 \cdots \beta_i \cdots \beta_x)$, $\boldsymbol{P}_{B\max} = diag(P_{B1\max} \cdots P_{Bi\max} \cdots P_{Bx\max})$, $\boldsymbol{\gamma} = diag(\gamma_1 \cdots \gamma_i \cdots \gamma_x)$, $\mathrm{SOC}_B = col(\mathrm{SOC}_{B1} \cdots \mathrm{SOC}_{Bi} \cdots \mathrm{SOC}_{Bx})$.

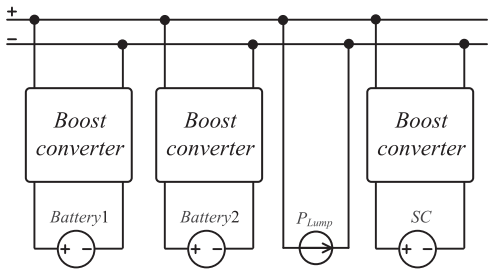

Fig. 5. A specific HESS with two batteries and a SC.

TABLE I
System Parameters

Parameters	Description	Value
V_{th}	Nominal bus voltage	170 V
m_1, m_2	V-P droop gain	0.01 V/W
n	ID droop gain	0.001π V/W
P_{Lump}	Lumped HESS load	1kW
P_{B1max}, P_{B2max}	Battery maximum output powers	1kW, 1kW
E_{B1}^{rate}, E_{B2}^{rate}	Battery rated energies	2kWh, 2kWh
E_{SC}^{rate}	SC rated energy	10^{-3}kWh
$\boldsymbol{L}$	Laplacian matrix	$[1\ -1; -1\ 1;]$

Note that the SOC of a battery is the function in terms of its output power. As such, SOC_B in (18) can also be arranged into s domain by properly manipulating (10), i.e.,

$$\mathrm{SOC}_B = \mathrm{SOC}_{B0} - (s\boldsymbol{I}_x)^{-1}(\boldsymbol{E}_B^{rate})^{-1}\boldsymbol{P}_B, \tag{19}$$

where $\mathrm{SOC}_{B0} = col(\mathrm{SOC}_{B10} \cdots \mathrm{SOC}_{Bi0} \cdots \mathrm{SOC}_{Bx0})$, $\boldsymbol{E}_B^{rate} = diag(E_{B1}^{rate} \cdots E_{Bi}^{rate} \cdots E_{Bx}^{rate})$. Substituting (19) into (18) results in

$$\boldsymbol{\varepsilon} = \boldsymbol{D}\boldsymbol{P}_B + \boldsymbol{C}\mathrm{SOC}_{B0}, \tag{20}$$

where $\boldsymbol{D} = \boldsymbol{B} - \boldsymbol{C}(s\boldsymbol{I}_x)^{-1}(\boldsymbol{E}_B^{rate})^{-1}$.

With the substitution of (17) and (20) into (15) and combining with (16), following equations governing the HESS system hold,

$$\begin{cases}
\mathbf{1}_x(V_b - V_{th}) = \boldsymbol{E}(\boldsymbol{D} - \boldsymbol{m})\boldsymbol{P}_B + \boldsymbol{E}\boldsymbol{C}\mathrm{SOC}_{B0}\\
\mathbf{1}_y(V_b - V_{th}) = -(s\boldsymbol{I}_y)^{-1}\boldsymbol{n}\boldsymbol{P}_{SC}\\
\mathbf{1}_x\boldsymbol{P}_B + \mathbf{1}_y\boldsymbol{P}_{SC} = P_{Lump}
\end{cases}, \tag{21}$$

where $\boldsymbol{E} = [diag(\mathbf{1}_x + \boldsymbol{A})]^{-1}$. It is possible to discern that the first two formulas in (21) contain entirely $x + y - 1$ independent equations. Together with the last algebraic expression, all elements in vectors $\boldsymbol{P}_B$ and $\boldsymbol{P}_{SC}$ have unique solutions. They can be depicted in s domain, which facilitates dynamic analyses for all signals inside the HESS system.

IV. System Dynamic Analyses

A HESS generic model consisting of x batteries and y SCs has been carefully derived Section III. To have a clearer view how electrical variables respond to load power change, a specific HESS comprising two batteries and a SC is considered in this section, see Fig. 5. Relevant system parameters have been summarized in Table I. For easy explanations, it is presumed that integration parameters α_i, β_i and γ_i in batteries are identically

set, i.e., $\alpha = \alpha_1 = \alpha_2$, $\beta = \beta_1 = \beta_2$ and $\gamma = \gamma_1 = \gamma_2$. Upon α, β and γ selected as 0.4, 200 and 50, appropriately substituting the above parameters into (21) and solving the equation yield,

$$P_{B1} = \frac{p_1(s)}{\Delta(s)} P_{Lump} + \frac{z_{11}(s)}{\Delta(s)} \mathrm{SOC}_{B10} + \frac{z_{12}(s)}{\Delta(s)} \mathrm{SOC}_{B20}, \tag{22}$$

$$P_{B2} = \frac{p_2(s)}{\Delta(s)} P_{Lump} + \frac{z_{21}(s)}{\Delta(s)} \mathrm{SOC}_{B10} + \frac{z_{22}(s)}{\Delta(s)} \mathrm{SOC}_{B20} \tag{23}$$

$$P_{SC} = \frac{p_{SC}(s)}{\Delta(s)} P_{Lump}, \tag{24}$$

where $\Delta(s)$ is the characteristic polynomial. $z_{12}(s) = z_{21}(s) = -z_{11}(s), z_{22}(s) = z_{11}(s)$. Detailed expressions of $\Delta(s), p_1(s), p_2(s), p_{SC}(s), z_{11}(s)$ have been provided below,

$$\begin{aligned}
\Delta(s) &= 5.184e^{15}s^{15} + 2.1476e^{17}s^4 + 3e^{17}s^3 \\
&\quad + 1.328^{17}s^2 + 2.1751e^{16}s + 1.4476e^{14}, \\
p_1(s) &= 5.184e^{14}\pi s^4 + 2.1358e^{16}\pi s^3 \\
&\quad + 2.0963e^{16}\pi s^2 + 3.4618e^{15}\pi s + 2.3e^{13}\pi, \\
p_2(s) &= 5.184e^{14}\pi s^4 + 2.1151e^{16}\pi s^3 \\
&\quad + 2.0963e^{16}\pi s^2 + 3.4618e^{15}\pi s + 2.3e^{13}\pi, \\
p_{SC}(s) &= 5.184e^{15}s^5 + 2.1151e^{17}s^4 + 1.6733e^{17}s^3 \\
&\quad + 1.152e^{15}s^2, \\
z_{11}(s) &= 5.184e^{21}s^4 + (4.1472e^{21} + 1.0368e^{21}\pi)s^3 \\
&\quad + 1.0365e^{21}\pi s^2 + 1.6589e^{20}\pi s.
\end{aligned}$$

A. Dynamics of Transient Power Sharing

It can be observed that P_1, P_2 and P_{SC} in equations (22)–(24) share a common characteristic denominator $\Delta(s)$ whose poles define the stability of HESS system. To understand how the transient power sharing happens between batteries and SC, it is assumed that battery initial SOCs, SOC_{10} and SOC_{20}, are the same. With this assumption, keeping in mind that $z_{11}(s) = -z_{12}(s)$ and $z_{21}(s) = -z_{22}(s)$, the last two items in (22) and (23) can be eliminated. Then P_1 and P_2 are reduced as

$$P_{B1} = \frac{p_1(s)}{\Delta(s)} P_{Lump} \Rightarrow \frac{P_{B1}}{P_{Lump}} = \frac{p_1(s)}{\Delta(s)}, \tag{25}$$

$$P_{B2} = \frac{p_2(s)}{\Delta(s)} P_{Lump} \Rightarrow \frac{P_{B2}}{P_{Lump}} = \frac{p_2(s)}{\Delta(s)}, \tag{26}$$

where $p_1(s)/\Delta(s)$ and $p_2(s)/\Delta(s)$ represent the transfer functions from P_{Lump} to P_1 and P_2 respectively. Together with the transfer function from P_{Lump} to P_{SC}, i.e., $p_{SC}(s)/\Delta(s)$, the pole-zero maps are plotted in Fig. 6, wherein the poles and zeros that have real parts less than -1 are not displayed as they would hardly affect HESS dynamics. All the roots of $\Delta(s)$ are confined in left half plane, which suggests that HESS imposed with the proposed semi-consensus strategy is a stable system. From Fig. 6, it is found that a pair of conjugate poles, $-0.3142 \pm j0.1642$, would dominate HESS performances, whereas for the rest poles, they are almost canceled by the accompanying zeros. At this point, the damping ratio ξ of HESS can be computed as,

$$\xi = \frac{0.3142}{\sqrt{0.3142^2 + 0.1642^2}} = 0.8863. \tag{27}$$

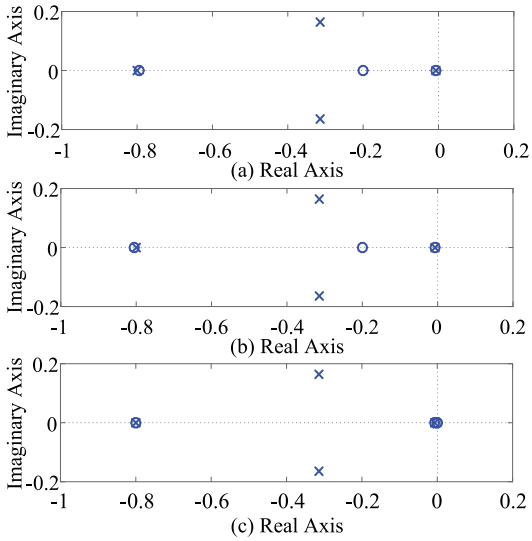

Fig. 6. Pole-zero maps for $p_1(s)/\Delta(s)$, $p_2(s)/\Delta(s)$ and $p_{SC}(s)/\Delta(s)$.

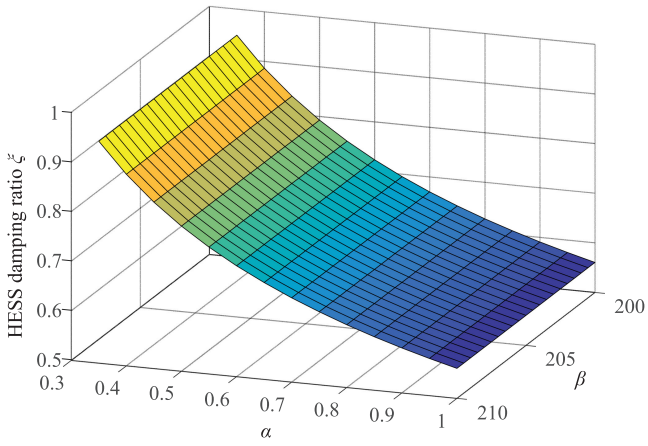

Fig. 7. HESS system damping with respect to α and β variations.

The ξ variation respect to the changes in α and β has been demonstrated in Fig. 7. The figure reveals that HESS damping would be decreased when the voltage control parameter α increases from 0.3 to 1, while the damping is nearly in no relation to β. For example, provided that α is selected as 0.5, the damping ratio keeps unchanged at around 0.8 despite of β varying from 200 to 210. This fact considerably boosts working efficiencies for engineering practitioners who make efforts to achieve desirable and stable dynamic power sharing in HESS as they only need to tune a single parameter α. For system damping improvement, α and β in this paper are assigned as 0.4 and 200 separately.

To investigate the transient power sharing between batteries and SC, the bode diagrams of transfer functions, $p_1(s)/\Delta(s)$ and $p_2(s)/\Delta(s)$, are displayed in Fig. (8) and Fig. (9). For Fig. 8, the increased α induces a minor magnitude resonance

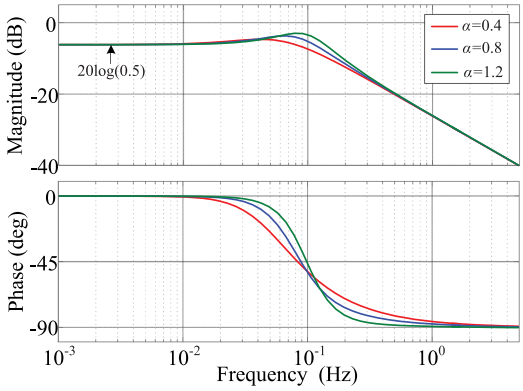

Fig. 8. Bode plot of $p_1(s)/\Delta(s)$ when $\alpha = 0.4$, 0.8 and 1.2, and $\beta = 200$.

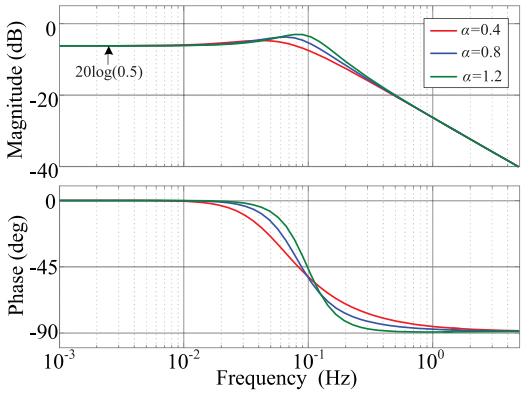

Fig. 9. Bode plot of $p_2(s)/\Delta(s)$ when $\alpha = 0.4$, 0.8 and 1.2, and $\beta = 200$.

of $p_1(s)/\Delta(s)$. In low frequency band, its magnitude could be estimated as $20\log(0.5) = -6.02$ dB, which means battery1 supplies half of the power demand (P_{Lump}). Similar results can also be found in Fig. (9) where battery2 refrains from responding to load power in high frequencies. The magnitude of $p_2(s)/\Delta(s)$ in low frequencies can be read as $20\log(0.5) = -6.02$ dB. In steady state, the equal power sharing of batteries has be realized. This is consistent with the expectation in Fig. 5 where the two batteries have the same droop coefficients and they are supposed to equally share the load power. Regarding the dynamics of SC power, the bode diagram of $p_{SC}(s)/\Delta(s)$ has been plotted in Fig. 10. The magnitude of $p_{SC}(s)/\Delta(s)$ keeps small in low frequencies. It reaches 0 dB from about 0.2 Hz to infinity, which indicates the SC compensates the entire load power in transient state while stops generating power in steady state.

It should be pointed that the battery powers and SC power are complementary to each other. Their combined powers would match the load demand in full frequency range. Step responses of P_{B1}, P_{B2} and P_{SC} are respectively shown in Fig. 11 when P_{Lump} is configured as 1 kW. At 0 s, in the case of $\alpha = 0.4$, SC immediately releases 1 kW power. After P_{SC} reduces to zero, SC continues to absorb power from the DC bus, hence entailing P_{SC} becoming a negative value. At the end of system transition, P_{SC} converges to zero. P_{B1} and P_{B2} slowly increase from 0 kW to 0.5 kW. As for other settings of lager α, more remarkable power overshoots are seen in P_{B1} and P_{B2}. Particularly for $\alpha = 1.2$, differing from the scenario with $\alpha = 0.4$, P_{SC} rises over zero,

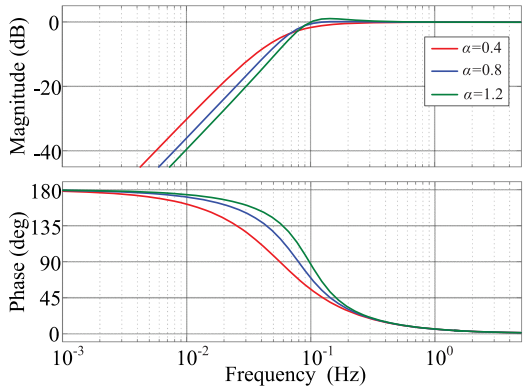

Fig. 10. Bode plot of $P_{SC}/\Delta(s)$ when $\alpha = 0.4$, 0.8 and 1.2, and $\beta = 200$.

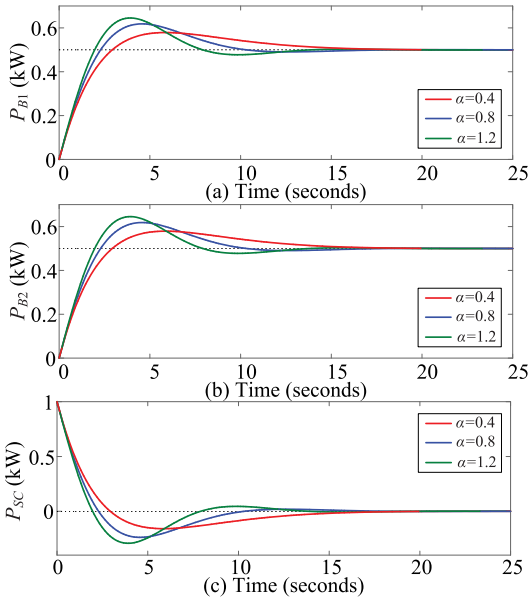

Fig. 11. Step responses of P_{B1}, P_{B2} and P_{SC} with different α and $\beta = 200$.

and SC is discharged again right after a complete discharging and charging process, which may unnecessarily increase SC microcycles shortening SC life time. Slight oscillations can also be found in P_{B1} and P_{B2}. These observations are in prefect agreement with the analyzing results in Figs. 8–10.

B. Dynamics of SC SOC

The power profile of SC under $\alpha = 0.4$ and $\beta = 200$ is further explicitly illustrated in Fig. 12(a). In transient state, SC is firstly discharged and then charged before its output power numerically settles down to zero. However, the sequential discharging and charging processes do not reflect the behaviors of stored energy in SC. To tackle this issue, the release energy by SC, which is defined as the time integration of P_{SC}, is displayed in Fig. 12(b) where the energy is found falling to zero after transient state. In this sense, revisiting Fig. 12(a), it can be inferred that the power-releasing and power-absorbing processes on P_{SC} have the equal areas. The energy escaping from SC will spontaneously flow back to maintain SC SOC at the original level. Writing SC

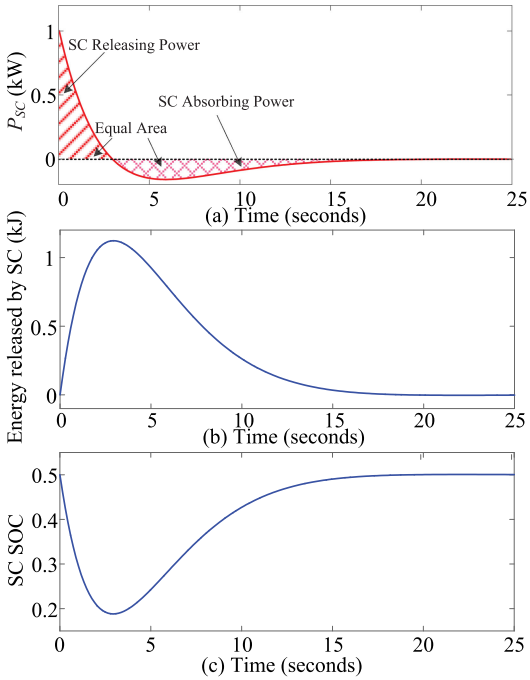

Fig. 12. Step responses of P_{SC} and SC SOC with $\alpha = 0.4$ and $\beta = 200$.

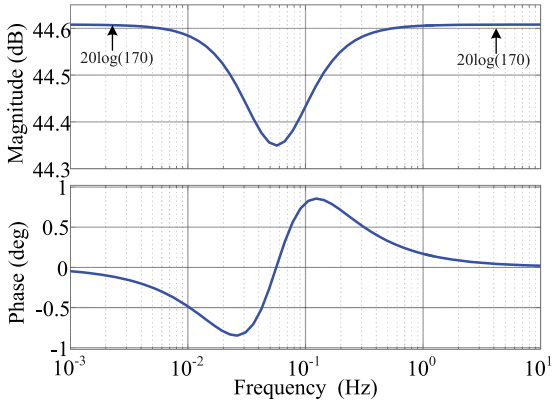

Fig. 13. Bode plot of V_b.

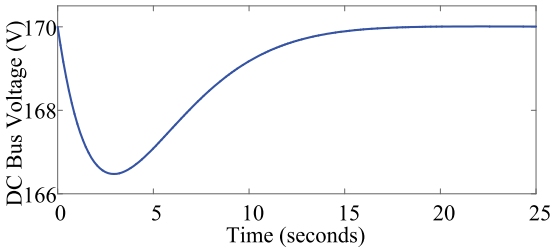

Fig. 14. Step response of V_b.

SOC definition of (13) into s domain where E_{SC}^{rate} is 10^{-3} kWh (see Table I) and initial SOC is assumed as 0.5, the step response of SC SOC is correspondingly depicted in Fig. 12(c). It is seen that SC SOC decreases to around 0.2 at 2.5 s and then recovers to 0.5 when system transition ends at 20 s, which attests to the function of spontaneous SC SOC restoration in HESS.

C. Dynamics of DC Bus Voltage

The power quantities of batteries and SC have been derived in (22)–(24). The s domain description of DC bus voltage V_b can also be deduced by referring to (16), i.e.,

$$V_b = V_{th} - \frac{n}{s} P_{SC} = V_{th} - \frac{n \cdot p_{SC}(s)}{s\Delta(s)} P_{Lump}. \tag{28}$$

The bode diagram and step response of (28) have been shown in Fig. 13 and Fig. 14. It is conspicuous from Fig. 13 that the voltage magnitude is 20log(170) = 44.61 dB in both low and high frequency bands, whereas there is a magnitude trap at roughly 0.05 Hz. This indicates V_b would decrease from 170 V at the instant when load change takes place, and the voltage is restored to 170 V in steady state. The indication can be substantiated by the step responses in Fig. 13 which firmly validates the HESS function of autonomous DC bus restoration.

D. Dynamics of Battery SOCs

Proceeding to scrutinize the battery SOC dynamics, in (22) and (23), P_{Lump} in this subsection is set as zero, while SOC_{B10} and SOC_{B20} are respectively assigned as 0.92 and 0.9. For this setting, (22) and (23) can be simplified below,

$$P_{B1} = \frac{z_{11}(s)}{\Delta(s)} \text{SOC}_{B10} + \frac{z_{12}(s)}{\Delta(s)} \text{SOC}_{B20}, \tag{29}$$

$$P_{B2} = \frac{z_{21}(s)}{\Delta(s)} \text{SOC}_{B10} + \frac{z_{22}(s)}{\Delta(s)} \text{SOC}_{B20}. \tag{30}$$

Substituting (29) and (30) into (10) yields battery SOCs,

$$\text{SOC}_{B1} = \left(1 - \frac{z_{11}(s)}{sE_{B1}^{rate}\Delta(s)}\right) \text{SOC}_{B10} - \frac{z_{12}(s)}{sE_{B1}^{rate}\Delta(s)} \text{SOC}_{B20}, \tag{31}$$

$$\text{SOC}_{B2} = -\frac{z_{21}(s)}{sE_{B2}^{rate}\Delta(s)} \text{SOC}_{B10} + \left(1 - \frac{z_{22}(s)}{sE_{B2}^{rate}\Delta(s)}\right) \text{SOC}_{B20}. \tag{32}$$

Bode diagrams of (31) and (32) have been provided in Fig. 15 where the magnitudes of SOC_{B10} and SOC_{B20} are 20log(0.92) = −0.724 dB and 20log(0.9) = −0.915 dB respectively in the range of high frequencies. In low frequency band, two SOCs are equalized at 20log(0.91) = −0.82 dB, which foretells that battery SOCs will be the same in steady state. SOC step responses in time domain are plotted in Fig. 16. It is seen that, under the proposed semi-consensus strategy, SOC_{B1} and SOC_{B2} converge to 0.91 at around 600 s, hence balancing battery SOCs in HESS.

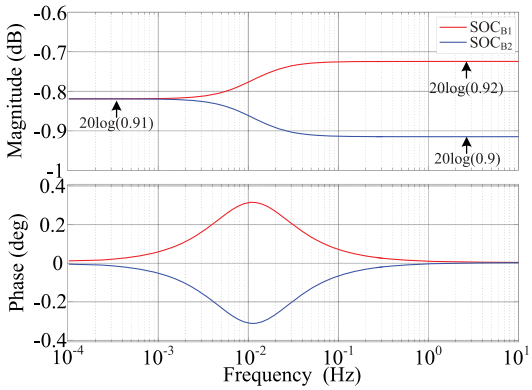

Fig. 15. Bode plots of SOC_{B1} and SOC_{B2} with their initial values being 0.92 and 0.9 respectively.

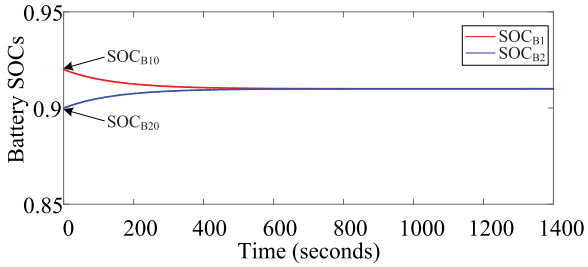

Fig. 16. Step responses of SOC_{B1} and SOC_{B2} with their initial values being 0.92 and 0.9 respectively.

V. Discussions

A. Cooperation With Higher Supervisory Controller

For HESS itself, the proposed semi-consensus control scheme realizes the four objectives, i.e., transient power allocation between batteries and SCs, autonomous DC bus recovery, spontaneous SC SOC recovery, and autonomous battery SOC balancing. Along with the realizations of these objectives, the power flow inside the HESS has been naturally and uniquely determined. If the HESS is connected to a main large scale power system with a supervisory controller, then a power converter module interlinks the HESS with the main should be used. The converter can respond to power reference sent from the supervisory controller, which helps to achieve the entire system economic operations.

B. Overcoming Line Impedance Impacts

In the DC system, there would exist line impedance. Regarding the impedance between converters and the DC bus, as in [22], [23], virtual impedance controllers can be integrated into the converter controls to fully neutralize the line impedance impacts. Moreover, it is seen from Fig. 4 that the proposed local distributed regulator is in no relation to any line impedance. Hence, the desired multi-functional HESS performances will not be impaired by line impedance at all.

C. Comparison With Other Approaches

Firstly, compared with the decentralized methods in [2], [4]–[6] where DC bus voltage is floating and only one control objective is achieved, the proposed semi-consensus strategy restores the HESS bus voltage to its nominal value and also enables multiple HESS functions, as listed in Section I. Secondly, for those centralized controls [7]–[10], they need a central controller to collect data across the whole system. While processing the data, intensive computational burdens would be incurred in the central controller, and the centralized schemes are also universally castigated being vulnerable to single-point-failures. In contrast, the semi-consensus method employs distributed communications which elude the central controllers and enhance overall system scalability. Thirdly, in [14]–[17], although distributed controls are applied to DC systems, similar to those decentralized mechanisms, only single control objective is attained, and no transient power sharing in HESS is accomplished. Differently, the proposed semi-consensus does bolster multi-functional HESS operations. The communication links in SCs are also avoided, which helps to truncate system investment costs.

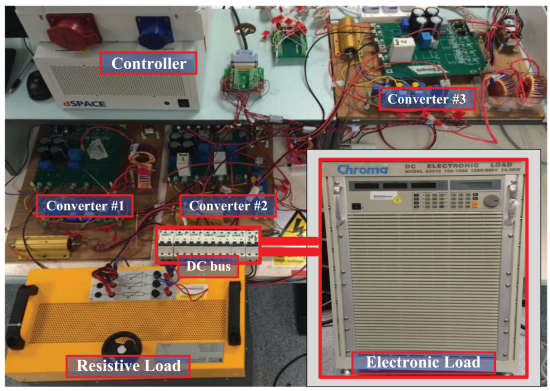

Fig. 17. An in-house hardware platform.

VI. Experiments

To corroborate the proclaimed multiple functions of HESS regulated by the proposed semi-consensus strategy, an in-house hardware platform is established in Fig. 17. The platform one-line diagram has been illuminated in Fig. 5. Converter #1 and converter #2 are interfaced with lead acid batteries and converter #3 is with a SC. Dspace1006 would generate PWM signals to control three boost converters. A resistive load and an electronic load are coupled to the common DC bus. For the converters per se, the inductance and capacitance are designed as 2 mH and 470 uF separately. Other parameters regarding droop controllers and nominal voltage level are all the same as in Table I.

A. Case 1: System Initialization With Battery SOC Balancing

To substantiate the effectiveness of battery SOC balancing, for the system in Fig. 17, only resistive load of 100 Ω is enabled while the electronic load is in standby mode. The initial battery SOCs, SOC_{B10} and SOC_{B20}, are differently set as 0.92 and 0.9 respectively. In this situation, imposed by semi-consensus strategy, the battery with higher SOC should output more power and charge another battery. The experimental results of around 20 minutes are recorded in Fig. 18. It is imperative to explain that SOC balancing process in batteries has a rather long time

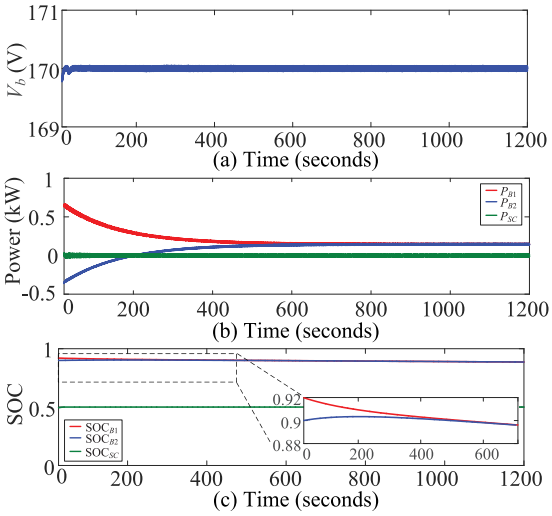

Fig. 18. System initialization with battery SOC balancing (Data are sampled by Dspace1006).

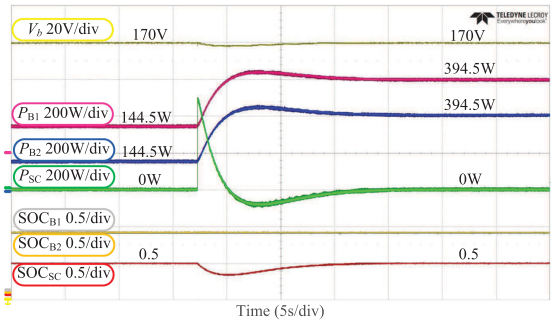

Fig. 19. HESS under discharging process.

such that the SOC dynamics cannot be captured by oscilloscope. Hence, the signals of interest are sampled by Dspace1006 and then plotted in Matlab environment. In Fig. 18, along the initialization process, the DC bus voltage is consistently maintained at 170 V. Once the local distributed compensatory is activated, P_{B1} immediately surges to near 0.65 kW and P_{B2} falls to -0.35 kW. They eventually converge to the same value of about 0.145 kW and realize equal power sharing among batteries as expected in Table I. Since there is no sudden load change, the SC power keeps at zero for the whole duration and SC SOC also remains invariant at its initial value 0.5. It is evident from Fig 18(c) that the two SOCs are equalized at roughly 600 s in spite of the initial SOC differences, which means the SOC balancing between batteries has been favorably accomplished. For safe operations, the minimum and maximum battery SOCs are set as 0.1 and 0.95 respectively, and it will be found that the battery SOCs in the following discharging/charging processes will always be constrained in the allowable range.

B. Case 2: HESS With Discharging Process

Following Case 1, Case 2 investigates the HESS performances when the lumped system load is increased abruptly. In Fig. 19, before load stepup, V_b can be read as 170 V. P_{B1} and P_{B2} are respectively approximated as 144.5 W. In steady state, P_{SC} is 0 W and SC SOC is 0.5. When the electronic load serving as a 500 W CPL is configured, SC instantly release power of 500 W compensating the high frequency components of load power. SC power gradually decreases zero and then a negative value, which indicates that the SC is absorbing power from the DC bus. SC power finally stabilizes at 0 W in steady state, and SC SOC returns 0.5 although there is a remarkable debasement in transient state. As for battery powers, they reach to new level of 394.5 W after system transition. The equal power sharing of batteries is perfectly attained in both transient and steady states, and battery SOC balancing achieved by Case 1 is little affected.

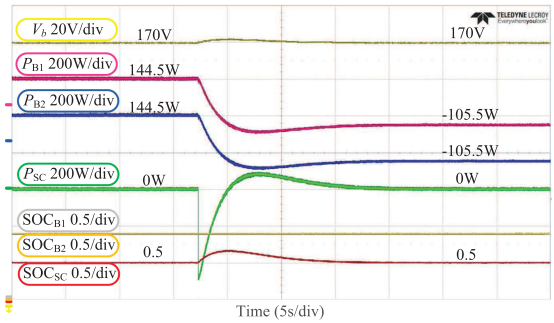

Fig. 20. HESS under charging process.

C. Case 3: HESS With Charging Process

Unlike the previous two cases, Case 3 would probe into the scenario that the whole HESS system is in charging process. For this case, the electronic load is displaced by a current source acting as a constant power source (CPS) that injects 500 W into DC bus. Notice that the injected power has completely covered the power requested by the resistive load ($170^2/100 = 289$ W). The remaining power ($500 - 289 = 211$ W) would be autonomously diverted to HESS and stored in them. From Fig. 20, at the instant of CPS being enabled, SC quickly ingests power up to 500 W to mitigate the impacts of unexpected load change on batteries. SC power slowly grows to zero and subsequently a positive value, which means the SC is discharging right after the exigent charging process. At the end of transient state, SC power declines to zero, and SC SOC is also brought back to the initial value while a considerable SOC increment is found during system transition. To consume the excessive power induced in the system, P_{B1} and P_{B2} reverse to negative quantities, i.e., -105.5 W from 144.5 W. The both batteries are in charging modes and the excessive power produced by CPS can still be equally shared. For the battery SOCs, they are always equalized at the same level. The DC bus voltage is desirably stabilized at 170 V in steady state.

VII. Conclusion

This paper presents a novel semi-consensus strategy to realize multi-functional HESS energy management. In the strategy, each battery is equipped with a local distributed compensator

which generates correction items to revise battery V-P droops. Compared with batteries which need data exchanging processes, SCs with ID controller do not involve any communication links, which considerably reduces system capital costs. The coexistence of V-P and ID droops would automatically realize transient power allocation: distributing low frequency components of load power to batteries and high frequency components to SCs. Moreover, the proposed strategy also helps to realize other functions including autonomous DC bus voltage recovery, spontaneous SC SOC restoration, autonomous power sharing and SOC balancing in batteries. All these functions enable effective management in HESSs, potentially prolonging overall HESS useful life. Dynamic analyses attest to the feasibility of the semi-consensus strategy. Hardware experimentations perfectly match the theoretical analyses and substantiate the HESS multi-functional operations.

REFERENCES

[1] C. Jin, P. Wang, J. Xiao, Y. Tang, and F. H. Choo, "Implementation of hierarchical control in DC microgrids," *IEEE Trans. Ind. Electron.*, vol. 61, no. 8, pp. 4032–4042, Aug. 2014.

[2] Y. Gu, W. Li, and X. He, "Frequency-coordinating virtual impedance for autonomous power management of DC microgrid," *IEEE Trans. Power Electron.*, vol. 30, no. 4, pp. 2328–2337, Apr. 2015.

[3] J. Xiao, P. Wang, and L. Setyawan, "Multilevel energy management system for hybridization of energy storages in DC microgrids," *IEEE Trans. Smart Grid*, vol. 7, no. 2, pp. 847–856, Mar. 2016.

[4] P. Lin, P. Wang, J. Xiao, J. Wang, C. Jin, and Y. Tang, "An integral droop for transient power allocation and output impedance shaping of hybrid energy storage system in DC microgrid," *IEEE Trans. Power Electron.*, vol. 33, no. 7, pp. 6262–6277, Jul. 2018.

[5] Y. Zhang and Y. W. Li, "Energy management strategy for supercapacitor in droop-controlled DC microgrid using virtual impedance," *IEEE Trans. Power Electron.*, vol. 32, no. 4, pp. 2704–2716, Apr. 2017.

[6] Q. Xu, J. Xiao, P. Wang, X. Pan, and C. Wen, "A decentralized control strategy for autonomous transient power sharing and state-of-charge recovery in hybrid energy storage systems," *IEEE Trans. Sustain. Energy*, vol. 8, no. 4, pp. 1443–1452, Oct. 2017.

[7] Amin, R. T. Bambang, A. S. Rohman, C. J. Dronkers, R. Ortega, and A. Sasongko, "Energy management of fuel cell/battery/supercapacitor hybrid power sources using model predictive control," *IEEE Trans. Ind. Inform.*, vol. 10, no. 4, pp. 1992–2002, Nov. 2014.

[8] J. Xiao, P. Wang, L. Setyawan, and Q. Xu, "Multi-level energy management system for real-time scheduling of DC microgrids with multiple slack terminals," *IEEE Trans. Energy Convers.*, vol. 31, no. 1, pp. 392–400, Mar. 2016.

[9] B. Wang, U. Manandhar, X. Zhang, H. B. Gooi, and A. Ukil, "Deadbeat control for hybrid energy storage systems in DC microgrids," *IEEE Trans. Sustain. Energy*, to be published, doi: 10.1109/TSTE.2018.2873801.

[10] X. Zhang, B. Wang, U. Manandhar, H. B. Gooi, and G. Foo, "A model predictive current controlled bidirectional three-level DC/DC converter for hybrid energy storage system in DC microgrids," *IEEE Trans. Power Electron.*, vol. 34, no. 5, pp. 4025–4030, May 2019, doi: 10.1109/TPEL.2018.2873765.

[11] H. F. Habib, C. R. Lashway, and O. A. Mohammed, "A review of communication failure impacts on adaptive microgrid protection schemes and the use of energy storage as a contingency," *IEEE Trans. Ind. Appl.*, vol. 54, no. 2, pp. 1194–1207, Mar. 2018.

[12] P. Lin, C. Zhang, J. Wang, C. Jin, and P. Wang, "On autonomous large signal stabilization for islanded multi-bus dc microgrids: A uniform non-smooth control scheme," *IEEE Trans. Ind. Electron.*, to be published, doi: 10.1109/TIE.2019.2931281.

[13] P. Lin *et al.*, "A distributed power management strategy for multi-paralleled bidirectional interlinking converters in hybrid AC/DC microgrids," *IEEE Trans. Smart Grid*, vol. 10, no. 5, pp. 5696–5711, Sep. 2019, doi: 10.1109/TSG.2018.2890420.

[14] X. Chen *et al.*, "Distributed cooperative control of multiple hybrid energy storage systems in a DC microgrid using consensus protocol," *IEEE Trans. Ind. Electron.*, to be published, doi: 10.1109/TIE.2019.2898606.

[15] X. Chen, M. Shi, H. Sun, Y. Li, and H. He, "Distributed cooperative control and stability analysis of multiple DC electric springs in DC microgrid," *IEEE Trans. Ind. Electron.*, vol. 65, no. 7, pp. 5611–5622, Jul. 2018.

[16] F. Guo, Q. Xu, C. Wen, L. Wang, and P. Wang, "Distributed secondary control for power allocation and voltage restoration in islanded DC microgrids," *IEEE Trans. Sustain. Energy*, vol. 9, no. 4, pp. 1857–1869, Oct. 2018.

[17] X.-K. Liu, H. He, Y.-W. Wang, Q. Xu, and F. Guo, "Distributed hybrid secondary control for a DC microgrid via discrete-time interaction," *IEEE Trans. Energy Convers.*, vol. 33, no. 4, pp. 1865–1875, Dec. 2018.

[18] Y. Wang *et al.*, "Aggregated energy storage for power system frequency control: A finite-time consensus approach," *IEEE Trans. Smart Grid*, vol. 10, no. 4, pp. 3675–3686, Jul. 2019.

[19] X. Chen *et al.*, "Consensus based distributed control for photovoltaic-battery units in a DC microgrid," *IEEE Trans. Ind. Electron.*, vol. 66, no. 10, pp. 7778–7787, Oct. 2019.

[20] X. Wang, H. Zhang, and C. Li, "Distributed finite-time cooperative control of droop-controlled microgrids under switching topology," *IET Renewable Power Gener.*, vol. 11, no. 5, pp. 707–714, 2016.

[21] S. Bacha, I. Munteanu, and A. I. Bratcu, *Power Electronic Converters Modeling and Control* (Advanced Textbooks in Control and Signal Processing). London, U.K.: Springer, 2014. [Online]. Available: http://link.springer.com/10.1007/978-1-4471-5478-5

[22] P. Lin, C. Zhang, P. Wang, and J. Xiao, "A decentralized composite controller for unified voltage control with global system large-signal stability in DC microgrids," *IEEE Trans. Smart Grid*, to be published.

[23] P. Wang, C. Jin, D. Zhu, Y. Tang, P. C. Loh, and F. H. Choo, "Distributed control for autonomous operation of a three-port AC/DC/DS hybrid microgrid," *IEEE Trans. Ind. Electron.*, vol. 62, no. 2, pp. 1279–1290, Feb. 2015.

Pengfeng Lin (S'16) received the B.S. and M.S. degrees in electrical engineering from Southwest Jiaotong University, Chengdu, China, in 2013 and 2015, respectively. He is currently working toward the Ph.D. degree with the Interdisciplinary Graduate School, Energy Research Institute, Nanyang Technological University, Singapore. His research interests include energy storage systems, hybrid ac/dc microgrids, and electrical power system stability/reliability analyses.

Tianyang Zhao (M'18) received the B.Eng., M.Eng., and Ph.D. degrees in electrical engineering from North China Electric Power University, Beijing, China, in 2011, 2013, and 2017, respectively. He is currently a Postdoctoral Research Fellow with the Energy Research Institute, Nanyang Technological University, Singapore. His research interests include power system operation optimization, reliability, and game theory.

Benfei Wang (S'12–M'17) received the B.Sc. degree in electronic information science and technology from the University of Science and Technology of China, Hefei, China, in 2011, and the Ph.D. degree from Nanyang Technological University (NTU), Singapore, in 2017. From 2017 to 2019, he was a Postdoc Research Fellow with the Energy Research Institute, NTU. He is currently an Associate Professor with the School of Intelligent Systems Engineering, Sun Yat-sen University, Shenzhen, China. His research interests include model predictive control, multi-port converters, hybrid energy storage system, electric vehicles, and microgrids.

Yu Wang (S'12–M'17) received the B.Eng. degree from Wuhan University, Wuhan, China, in 2011, and the M.Sc. and Ph.D. degrees from Nanyang Technological University, Singapore, in 2012 and 2017, respectively. He is currently a Research Fellow with Nanyang Technological University. His research interests include distributed control and optimization, grid energy storage systems, renewable energy integration, microgrids, and smart grids.

Peng Wang (M'00–SM'11–F'18) received the B.Sc. degree from Xi'an Jiaotong University, Xi'an, China, in 1978, the M.Sc. degree from Taiyuan University of Technology, Taiyuan, China, in 1987, and the M.Sc. and Ph.D. degrees from the University of Saskatchewan, Saskatoon, SK, Canada, in 1995 and 1998, respectively. He is currently a Professor of Nanyang Technological University, Singapore.